Electronic Supplementary Information (ESI)

A first-principles study of diffusion coefficients of alloying elements in dilute α-Ti alloys

W. W. Xu,[abc] S. L. Shang,[c] B. C. Zhou,[c] Y. Wang,[c] L. J. Chen,[a] C. P. Wang,[bd] X. J. Liu,[*bd] and Z. K. Liu[c]

[a]*School of Aerospace Engineering, Xiamen University, Xiamen, 361005, P.R. China*

[b]*College of Materials, and Research Centre of Materials Design and Applications, Xiamen University, Xiamen, 361005, P.R. China*

[c]*Department of Materials Science and Engineering, Pennsylvania State University, University Park, Pennsylvania 16802, USA*

[d]*Fujian Key Laboratory of Materials Genome, Xiamen, 361005, P.R. China*

*Corresponding author: lxj@xmu.edu.cn (X. J. Liu)

Tel: +86-592-2187888; Fax: +86-592-2187966

1. Thermodynamic properties

As described in Section 2.2 of the manuscript, the lattice vibrational contribution to the Helmholtz free energy $F_{vib}(V, T)$ can be usually obtained from either the quasi-harmonic Debye or the quasi-harmonic phonon approach. In the phonon approach, $F_{vib}(V, T)$ is defined as [1]:

$$F_{vib}(V,T) = k_B T \int_0^{\infty} \ln[2\sinh\frac{\hbar\omega}{2k_B T}] g(\omega,V) d\omega \tag{1}$$

where g(ω,V) is the phonon density of states (DOS) at phonon frequency ω and volume V; $n(\varepsilon, V)$: the electronic density of states; f: the Fermi distribution; ε_F: the Fermi energy.

Based on phonon density of states, the *n*th moment Debye cutoff frequency and the corresponding *n*th moment Debye temperature can be determined, where the Debye cutoff frequencies are given by,

$$\omega_n = \left[\frac{n+3}{3}\int_0^{\omega_{\max}} \omega^n g(\omega) d\omega\right]^{1/n}, \text{ with } n \neq 0,\ n > \text{-}3 \tag{2}$$

$$\omega_0 = \exp\left[\frac{1}{3}\int_0^{\infty} \omega^n \ln(\omega) d\omega\right], \text{ with } n = 0 \tag{3}$$

Therefore the *n*th moment Debye temperature can be deduced by

$$\Theta_D(n) = \frac{\hbar}{k_B}\omega_n \tag{4}$$

In the Debye model, $F_{vib}(V, T)$ can be wrote as [1]:

$$F_{vib}(V,T) = \frac{9}{8}k_B\Theta_D + k_B T\left\{3\ln\left[1-\exp\left(-\frac{\Theta_D}{T}\right)\right] - D\left(\frac{\Theta_D}{T}\right)\right\} \tag{5}$$

where Θ_D is the Debye temperature; k_B the Boltzmann's constant; and the Debye function, $D(x)$, is given by $D(x) = 3/x^3\int_0^x z^3/[\exp(z)-1]dz$. To obtain $F_{vib}(V, T)$, Θ_D is the key value which can be calculated in terms of the Debye-Grüneisen approximation [2] by:

$$\Theta_D = sAV_0^{1/6}\left(\frac{B_0}{M}\right)^{1/2}\left(\frac{V_0}{V}\right)^{\gamma} \tag{6}$$

where A is a constant with $A = (6\pi^2)^{1/3}\hbar/k_B$; V_0 the equilibrium volume at 0 K; B_0 the bulk modulus; M the average atomic mass; γ the Grüneisen parameter, and s a parameter that scales the Debye temperature Θ_D.

Without using the Grüneisen parameter, Wang proposed a method (Debye-Wang model [3]) to calculated the Debye temperature [1]:

$$\Theta_D = sAV_0^{1/6}\left\{\frac{1}{M}\left[B - \frac{2(\lambda+1)}{3}P\right]\right\}^{1/2} \tag{7}$$

where the parameter λ in Debye-Wang model is an adjustable parameter.

In order to validate the applicability of Debye model adopted in this work, we calculated the Debye temperature using both Debye-Grüneisen and Debye-Wang models. Note that two different scaling factors s are performed when using Debye-Grüneisen model, with s = 0.617 obtained by Moruzzi [2] from nonmagnetic metals while s = 0.696 obtained from the Poisson's ratio of pure α-Ti [4, 5]. The results are tabulated in Table S1, together with the available measured data by Petry [6], and the DFT data from phonon calculations by Mei [7]. The results from the phonon calculation and Debye-Grüneisen model with s = 0.617 show an excellent consistent with the measurement (360 K [6]). While the Debye-Grüneisen model with s = 0.696 and Debye-Wang model largely overestimate the Debye temperature.

Then we computed the thermodynamic properties (*i.e.*, heat capacity C_p and entropy S) of pure α-Ti in terms of both Debye-Grüneisen model with two different scaling factors s (*i.e.*, 0.617 and 0.696) and Debye-Wang models, and illustrate the results in Figs. S1-S2. For comparison, the theoretical results from phonon calculation [7] and the experimental results [8-11] are also presented in Figs. S1-S2. Excellent agreement was achieved between computaion and experiments.

Therefore, for sake of simplicity and efficiency, the Debye-Grüneisen model with s = 0.617 was used in the present work to benchmark the Θ_D value of pure α-Ti from the experiment.

Table S1 Predicted Debye temperature (Θ_D) using both Debye-Grüneisen with two different scaling factors *s* (i.e., 0.617 and 0.696) and Debye-Wang models, together with the available experimental data [6] and the DFT data from phonon calculations [7].

properties	Debye-Grüneisen (This work)		Debye-Wang (This work)	Phonon (Mei)	Expt.
	s = 0.617	*s* = 0.696			
Θ_D (K)	361.4	407.6	372.8	359	360

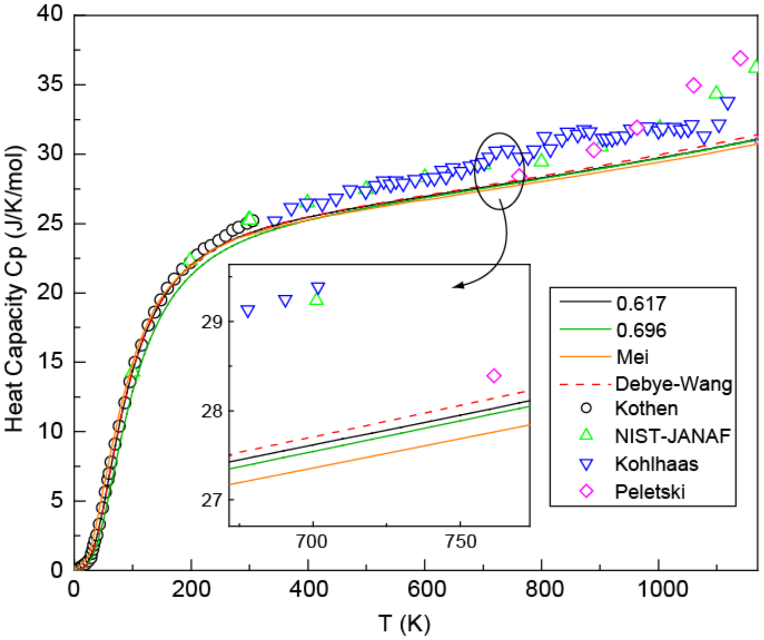

Fig. S1. Predicted heat capacity (C_p) of pure α-Ti as a function of temperature using the Debye-Grüneisen [1] (black and green solid lines) and Debye-Wang [1] (red dash lines) model, together with the measured data from NIST-JANAF [8], Kothen [9], Kohlhaas [10] and Peletski [11], and the DFT data from the quasi-harmonic phonon calculations by Mei [7].

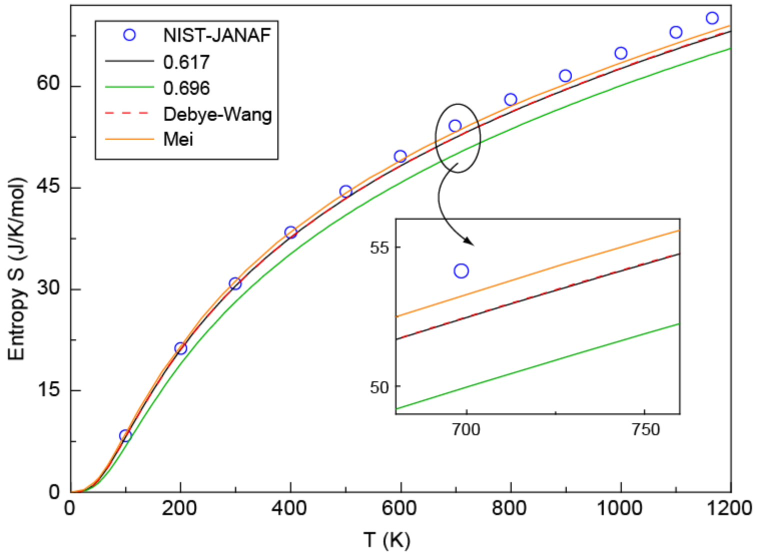

Fig. S2. Predicted entropy (*S*) of pure α-Ti as a function of finite temperatures using the Debye-Grüneisen [1] (black and green solid lines) and Debye-Wang [1] (red dash lines) model, together with the measured data from NIST-JANAF [8], and the DFT data from the quasi-harmonic phonon calculation by Mei [7]. Note that the entropy includes the lattice vibrational entropy (S_{vib}) and the thermal electronic contribution entropy (S_{ele}).

Table S2 First-principles predictions and experimental results of equilibrium lattice parameters (a_0, c_0, and V_0) for various solutes X (Al, V, Nb, Ta, Mo, Zr, and Sn) in dilute *α*-Ti.

Solutes	a_0 (Å)	c_0 (Å)	V_0 (Å^3/atom)	Ref.
Ti	2.899	4.592	16.705	This work
	2.951	4.674		Expt. [12]
	2.899	4.589		Calc. [13]
Al	2.897	4.589	16.673	This work
Ta	2.899	4.596	16.722	This work
Sn	2.900	4.604	16.761	This work
Nb	2.899	4.597	16.730	This work
Zr	2.904	4.597	16.794	This work
V	2.895	4.587	16.647	This work
Mo	2.895	4.595	16.670	This work

2. Minimum energy pathways

Figure S3 shows the predicted minimum energy pathways (MEP) for vacancy migration in pure α-Ti within the basal plane and between the adjacent basal planes using five images with the CI-NEB method. An anmalous energy pathway, with energetically equivalent double saddle points, is clear presented for MEP within the basal plane, which agree with the previous investigation by Shang [13]. The detailed discussion about this anmalous energy pathway of pure α-Ti can be seen in Ref. [13]. This anmalous MEP are also found for the solute diffusion of alloying elements in dilute α-Ti alloys. The predicted MEP for all solutes (i.e., Al, Zr, Sn, V, Ta, Nb, and Mo) diffusing in dilute α-Ti are illustrated in Figs. S4-10. Although the differece of migration energies for the double saddle points is very minor, it should be noticable that the maximum of them are chose as the migration barrier for the calculation of jump frequencies in the 8-frequency model.

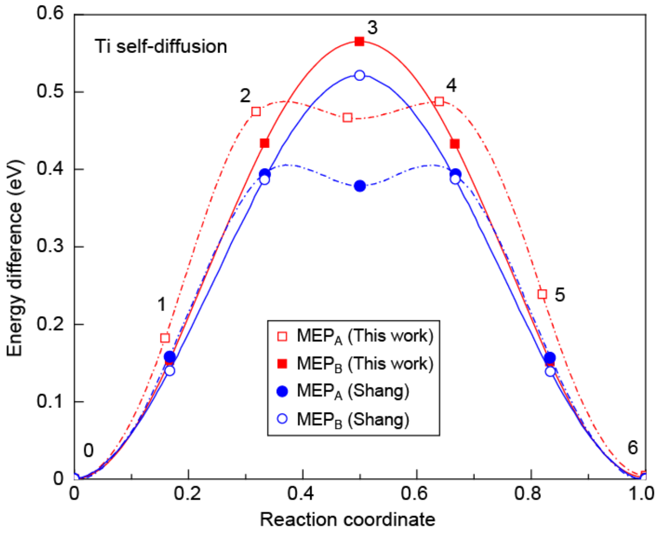

Fig. S3. Minimum energy pathways (MEP) of pure α-Ti within the basal plane and between the adjacent basal planes, together with the other DFT results by Shang [13]. The subscripts ''A'' and ''B'' represent the solute vacancy exchanges within a basal plane and between the basal planes, respectively, as shown in Fig. 1(b)-(c). Note that the numbers (*i.e.*, 1, 2, 3, 4, and 5) are corresponding to the number of Images adopted in the CI-NEB method, while the nmubers 0 and 6 represent the initial (**is**) and final (**FS**) states, respectively.

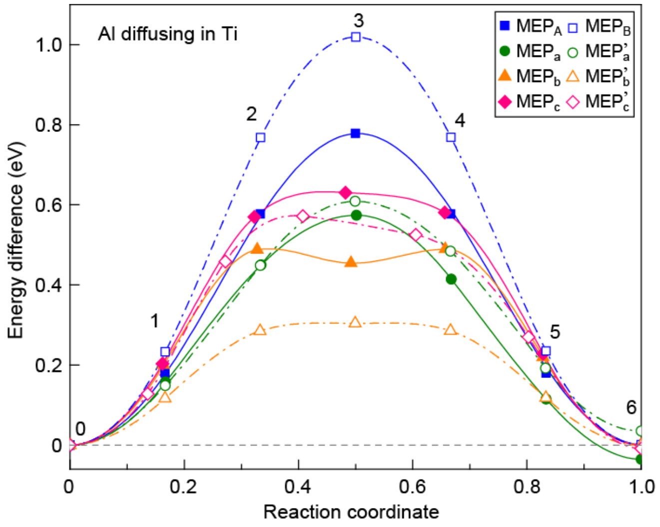

Fig. S4. Minimum energy pathways (MEP) of solute Al diffusing in dilute α-Ti within the basal plane and between the adjacent basal planes. The subscripts ''A" and "B" represent the solute vacancy exchange, and the subscripts "a", "b", "c", and "a'", "b'", "c'" represent the solvent vacancy exchange, respectively, as shown in Fig. 1(b)-(c). Note that the numbers (*i.e.*, 1, 2, 3, 4, and 5) are corresponding to the number of Images adopted in the CI-NEB method, while the nmubers 0 and 6 represent the initial (**is**) and final (**FS**) states, respectively.

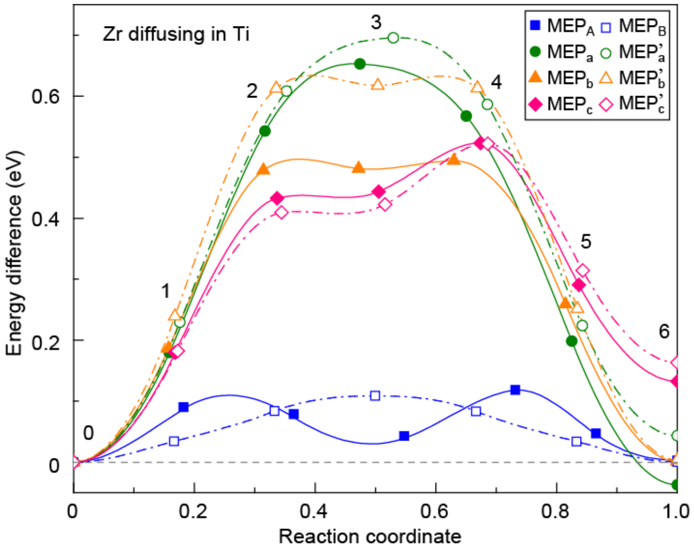

Fig. S5. Minimum energy pathways (MEP) of solute Zr diffusing in dilute α-Ti within the basal plane and between the adjacent basal planes. The subscripts ''A" and "B" represent the solute vacancy exchange, and the subscripts "a", "b", "c", and "a'", "b'", "c'" represent the solvent vacancy exchange, respectively, as shown in Fig. 1(b)-(c). Note that the numbers (*i.e.*, 1, 2, 3, 4, and 5) are corresponding to the number of Images adopted in the CI-NEB method, while the nmubers 0 and 6 represent the initial (**is**) and final (**FS**) states, respectively.

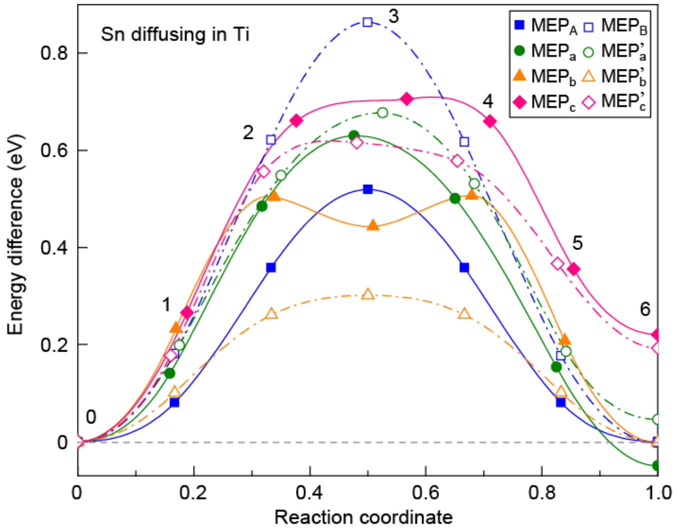

Fig. S6. Minimum energy pathways (MEP) of solute Sn diffusing in dilute α-Ti within the basal plane and between the adjacent basal planes. The subscripts ''A" and "B" represent the solute vacancy exchange, and the subscripts "a", "b", "c", and "a'", "b'", "c'" represent the solvent vacancy exchange, respectively, as shown in Fig. 1(b)-(c). Note that the numbers (*i.e.*, 1, 2, 3, 4, and 5) are corresponding to the number of Images adopted in the CI-NEB method, while the nmubers 0 and 6 represent the initial (**is**) and final (**FS**) states, respectively.

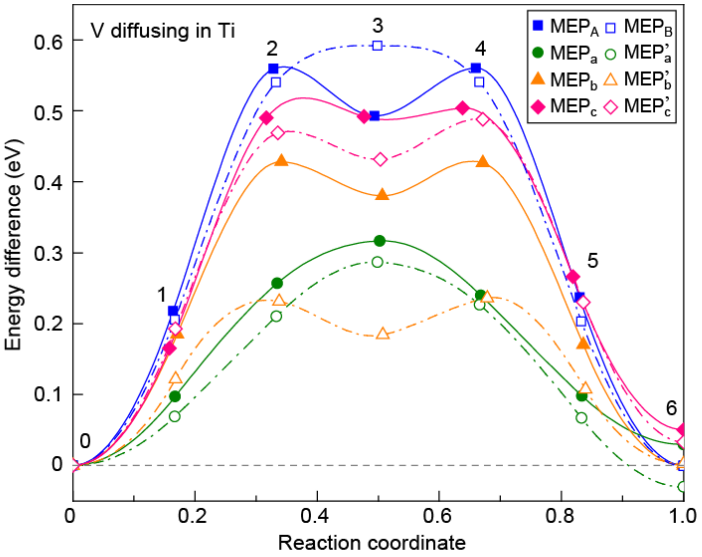

Fig. S7. Minimum energy pathways (MEP) of solute V diffusing in dilute α-Ti within the basal plane and between the adjacent basal planes. The subscripts ''A" and "B" represent the solute vacancy exchange, and the subscripts "a", "b", "c", and "a'", "b'", "c'" represent the solvent vacancy exchange, respectively, as shown in Fig. 1(b)-(c). Note that the numbers (*i.e.*, 1, 2, 3, 4, and 5) are corresponding to the number of Images adopted in the CI-NEB method, while the nmubers 0 and 6 represent the initial (**is**) and final (**FS**) states, respectively.

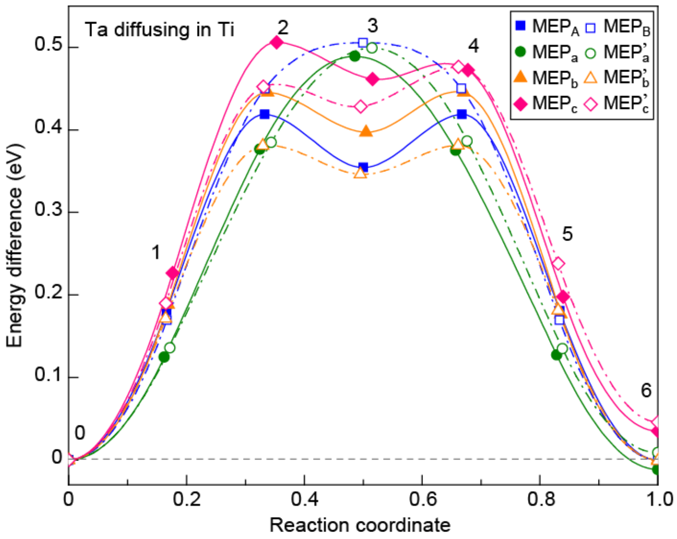

Fig. S8. Minimum energy pathways (MEP) of solute Ta diffusing in dilute α-Ti within the basal plane and between the adjacent basal planes. The subscripts ''A" and "B" represent the solute vacancy exchange, and the subscripts "a", "b", "c", and "a'", "b'", "c'" represent the solvent vacancy exchange, respectively, as shown in Fig. 1(b)-(c). Note that the numbers (*i.e.*, 1, 2, 3, 4, and 5) are corresponding to the number of Images adopted in the CI-NEB method, while the nmubers 0 and 6 represent the initial (**is**) and final (**FS**) states, respectively.

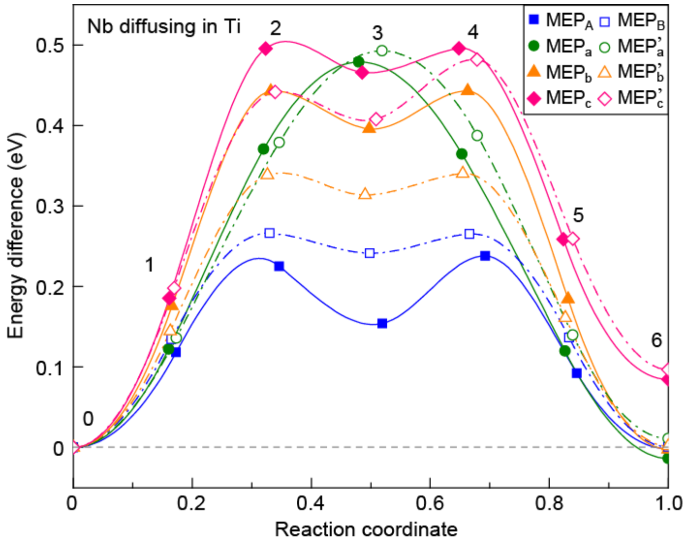

Fig. S9. Minimum energy pathways (MEP) of solute Nb diffusing in dilute α-Ti within the basal plane and between the adjacent basal planes. The subscripts ''A" and "B" represent the solute vacancy exchange, and the subscripts "a", "b", "c", and "a'", "b'", "c'" represent the solvent vacancy exchange, respectively, as shown in Fig. 1(b)-(c). Note that the numbers (*i.e.*, 1, 2, 3, 4, and 5) are corresponding to the number of Images adopted in the CI-NEB method, while the nmubers 0 and 6 represent the initial (**is**) and final (**FS**) states, respectively.

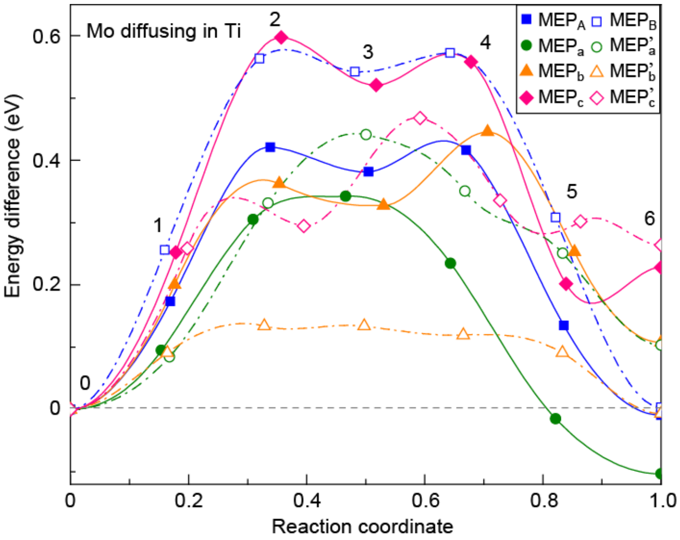

Fig. S10. Minimum energy pathways (MEP) of solute Mo diffusing in dilute α-Ti within the basal plane and between the adjacent basal planes. The subscripts "A" and "B" represent the solute vacancy exchange, and the subscripts "a", "b", "c", and "a'", "b'", "c'" represent the solvent vacancy exchange, respectively, as shown in Fig. 1(b)-(c). Note that the numbers (*i.e.*, 1, 2, 3, 4, and 5) are corresponding to the number of Images adopted in the CI-NEB method, while the nmubers 0 and 6 represent the initial (**is**) and final (**FS**) states, respectively.

3. Covalency and Cophonicity metric

According to the reports of Cammarata *et al.* [14, 15], the center mass CM of an atomic orbital $|n, l, m_l, m_s>$ for atom A is defined as

$$CM^A(n,l,m_l,m_s)=\frac{\int_{E_0}^{E_1} E g^A_{|n,l,m_l,m_s>}(E)dE}{\int_{E_0}^{E_1} g^A_{|n,l,m_l,m_s>}(E)dE} \tag{8}$$

Where n, l, m_l, and m_s represent the quantum number; $g^A(E)$ is the contribution of the atomic orbital $|n, l, m_l, m_s>$ of the atom A to the total electronic density of states (eDOS). The energy range $[E_0, E_1]$ in Eq. (8) is chosen in such a way that is encompasses all relevant bands participating in the bond. The relative position $C_{n1l1,n2l2}$ of the center mass of $|n_1, l_1>$ levels of atom A with respect to the center mass of $|n_2, l_2>$ levels of atom B is given as

$$C_{n_A l_A, n_B l_B}=-|CM^A(n_A,l_A)-CM^B(n_B,l_B)| \tag{9}$$

Accroding to the above definition, the relative position of the A levels with respect to the B levels is

$$C_{A,B}=-|CM(A)-CM(B)| \tag{10}$$

In this formalism, the greater the value of $C_{A,B}$, the higher the overlop of the selected atomic bands, implying a more covalenct A-B bond in the electron density. $C_{A,B} = 0$ would indicate the highest covalency achievable for the A-B bond in the geometric configuration of the crystal structure.

To show the relationship between diffusion properties and lattice vibrational features, a "cophonicity" descriptor formulated by Cammarata *et al* [16], based on dynamic properties of the solutes X and sovlent Ti atomic species, is adopted in the present work. The definition of cophonicity metric is similar to the covalency metric, which is closely related with the phonon density of states (pDOS) in the first Brillouim zone. According to Ref. [16], the center mass CM^A of the partial pDOS $[g^A(\omega)]$ of an atom A in defined as

$$CM^A=\frac{\int_{\omega_0}^{\omega_1}\omega g^A(\omega)d\omega}{\int_{\omega_0}^{\omega_1} g^A(\omega)d\omega} \tag{11}$$

where ω is the phonon frequency; $g^A(\omega)$ is the phonon contribution of the atom A to the total phonon density of states (pDOS). The intergration interval $[\omega_0, \omega_1]$ in Eq. (11) is chosen in such a way that is encompasses all pDOS relevant for the selected phonon band.

For a generic A-B atomic pair, the relative position C_{ph}(A-B) of the center mass of $g^{A}(\omega)$ with respect to the center mass of $g^{B}(\omega)$ is given as

$$C_{ph}(A-B) = CM^{A} - CM^{B} \tag{12}$$

In this formalism, the smaller the value of $|C_{ph}(\text{A-B})|$, the higher the mixing of the A and B contributions to the phonon frequency band. C_{ph}(A-B) = 0 would indicate the equal participation of both A and B atomic species to the formation of phonon states in the considered range of frequencies. Note that the more detailed description of mathematical implementation of covalency and cophonicity metric can be found in Refs. [14-16].

Based on the calculations of electornic density of states (eDOS) and phonon density of states (pDOS), the X-Ti bond Covalency metric $C_{\text{X-Ti}}$ and Cophonicity metric C_{ph} of the X-Ti pair for various solutes X (Al, Mo, and Zr) in dilute α-Ti are estimated and listed in Table S3. Note that two nearest neighbor Ti host atoms (*i.e.*, Ti1, Ti2) with the solute atom and the vacancy were considered here. Fig. S11 shows the calculated electronic density of states (eDOS) for various solutes X (Al, Mo, and Zr) in dilute α-Ti. Fig. S12 presents the calculated phonon dispersion curves and the relevant density of states (pDOS) along high-symmetry directions in the Brillouin zone for various solutes X (Al, Mo, and Zr) in dilute α-Ti, aided by the PHONOPY software [17]. Note that the substitution of one solute atom reduces the symmetries of the system, producing the splitting of those vibrational modes that were degenerate in the parent α-Ti structure as seen in Fig. S12.

Table S3 Calculated X-Ti Bond Covalency $C_{\text{X, Ti}}$ (eV), Cophonicity C_{ph} (THz) of the X-Ti pair for various solutes X (Al, Mo, and Zr) in dilute α-Ti.

	Covalency Metric					Cophonicity Metric				
	CM(X)	*CM*(Ti1)	*CM*(Ti2)	$C_{\text{X-Ti1}}$	$C_{\text{X-Ti2}}$	CM^{X}	CM^{Ti1}	CM^{Ti2}	C_{ph1}	C_{ph2}
Al	-2.01	-1.29	-1.25	-0.72	-0.76	7.73	5.56	5.34	2.17	2.39
Mo	-2.44	-1.15	-1.14	-1.29	-1.30	3.65	5.76	4.97	-2.11	-1.32
Zr	-2.16	-1.12	-1.13	-1.04	-1.03	4.02	5.42	5.59	-1.40	-1.57

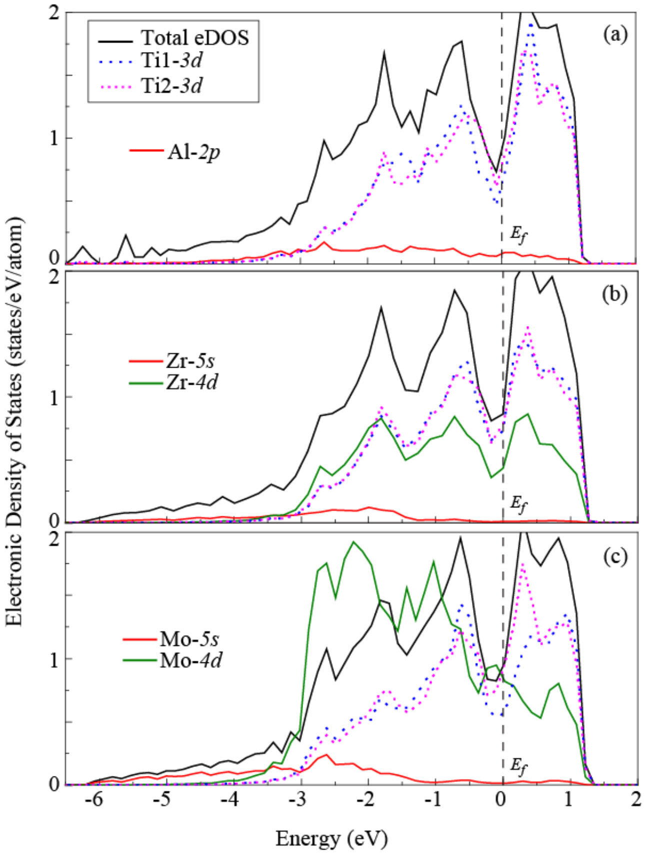

Fig. S11. Calculated electronic density of states (eDOS) for various solutes X (Al, Mo, and Zr) in dilute α-Ti: (a) X = Al, (b) X = Zr, (c) X = Mo. Note that the Fermi level (E_f) is indicated by the dashed vertical line at 0 eV.

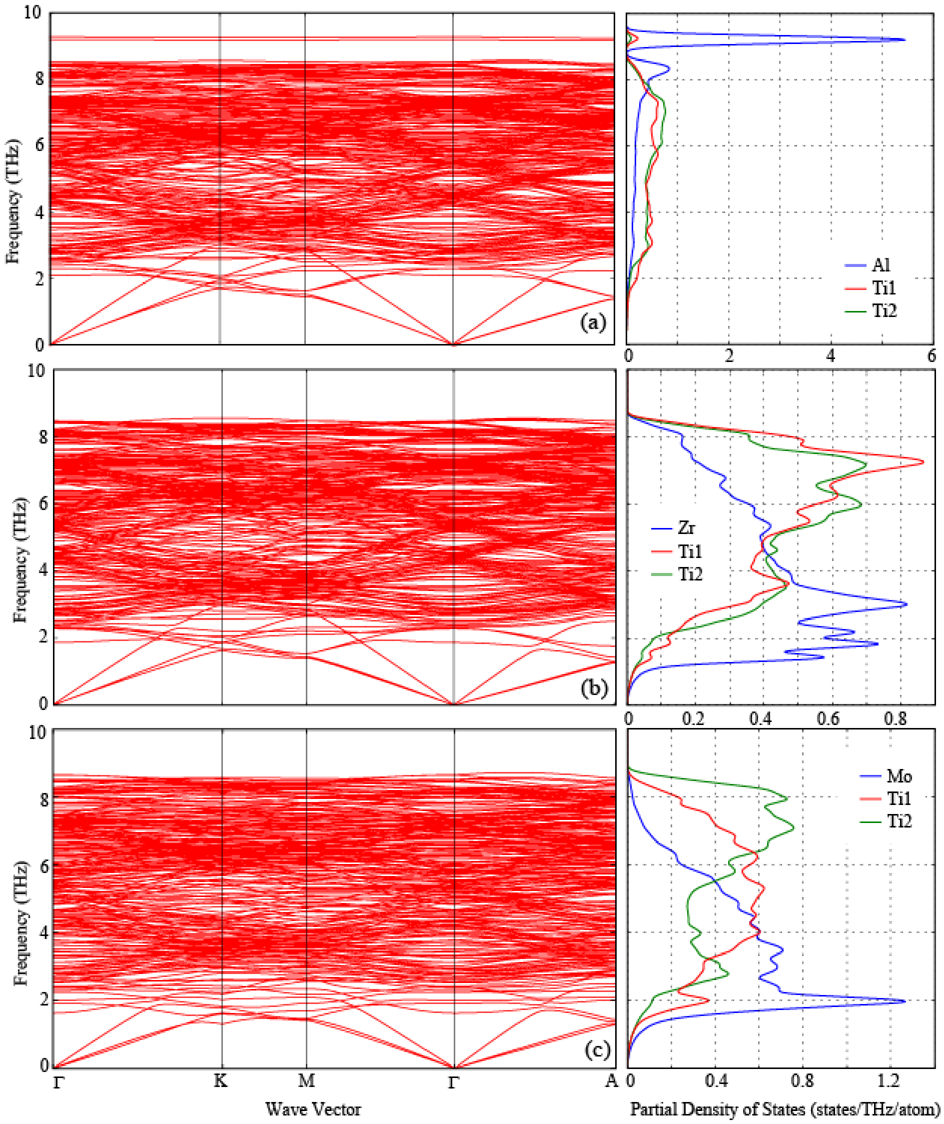

Fig. S12. Calculated phonon dispersion curves and the relevant density of states (pDOS) along high-symmetry directions in the Brillion zone for various solutes X (Al, Mo, and Zr) in dilute *α*-Ti. Note that the high-symmetry points in units of 2π/*a* are Γ (0, 0, 0), K (1/3, 1/3, 0), M (1/2, 0, 0), Γ (0, 0, 0), A (0, 0, 1/2), respectively.

References

[1] S.-L. Shang, Y. Wang, D. Kim, Z.-K. Liu. First-principles thermodynamics from phonon and Debye model: Application to Ni and Ni3Al, Comp. Mater. Sci. 47 (2010) 1040-1048.

[2] V.L. Moruzzi, J.F. Janak, K. Schwarz. Calculated thermal properties of metals, Phys. Rev. B 37 (1988) 790-799.

[3] Y. Wang, R. Ahuja, B. Johansson. Mean-field potential approach to the quasiharmonic theory of solids, Int. J. Quantum. Chem. 96 (2004) 501-506.

[4] X.L. Liu, B.K. VanLeeuwen, S.-L. Shang, Y. Du, Z.-K. Liu. On the scaling factor in Debye-Grüneisen model: A case study of the Mg-Zn binary system, Comp. Mater. Sci. 98 (2015) 34-41.

[5] S.L. Shang, A. Saengdeejing, Z.G. Mei, D.E. Kim, H. Zhang, S. Ganeshan, Y. Wang, Z.K. Liu. First-principles calculations of pure elements: Equations of state and elastic stiffness constants, Comp. Mater. Sci. 48 (2010) 813-826.

[6] W. Petry, A. Heiming, J. Trampenau, M. Alba, C. Herzig, H.R. Schober, G. Vogl. Phonon dispersion of the bcc phase of group-IV metals. I. bcc titanium, Phys. Rev. B 43 (1991) 10933-10947.

[7] Z.-G. Mei, S.-L. Shang, Y. Wang, Z.-K. Liu. Density-functional study of the thermodynamic properties and the pressure-temperature phase diagram of Ti, Phys. Rev. B 80 (2009) 104116.

[8] M.W. Chase. NIST-JANAF Thermochemical Tables, American Institute of Physics, Washington, D. C., 1998.

[9] C.W. Kothen, H.L. Johnston. Low Temperature Heat Capacities of Inorganic Solids. XVII. Heat Capacity of Titanium from 15 to 305°K.1, J. Am. Chem. Soc. 75 (1953) 3101-3102.

[10] W. Bendick, W. Pepperhoff. The heat capacity of Ti, V and Cr, J. Phys. F. 12 (1982) 1085.

[11] K.D. Maglić, D.Z. Pavičić. Thermal and Electrical Properties of Titanium Between 300 and 1900 K, Int. J. Thermophys. 22 (2001) 1833-1841.

[12] P. Villars, L.D. Calvert. Pearson's handbook of crystallographic data for intermetallic phases, ASTM International, Newbury, OH, 1991.

[13] S.L. Shang, L.G. Hector, Y. Wang, Z.K. Liu. Anomalous energy pathway of vacancy migration and self-diffusion in hcp Ti, Phys. Rev. B 83 (2011) 224104.

[14] A. Cammarata, W. Zhang, P.S. Halasyamani, J.M. Rondinelli. Microscopic Origins of Optical Second Harmonic Generation in Noncentrosymmetric–Nonpolar Materials, Chem. Mater. 26 (2014) 5773-5781.

[15] A. Cammarata, J.M. Rondinelli. Covalent dependence of octahedral rotations in orthorhombic perovskite oxides, The Journal of Chemical Physics 141 (2014) 114704.

[16] A. Cammarata, T. Polcar. Tailoring Nanoscale Friction in MX2 Transition Metal Dichalcogenides, Inorg. Chem. 54 (2015) 5739-5744.

[17] A. Togo, I. Tanaka. First principles phonon calculations in materials science, Scripta Mater. 108 (2015) 1-5.